

H₂ distribution during formation of multiphase molecular clouds

Valeska Valdivia^{1,2,3}, Patrick Hennebelle^{2,1}, Maryvonne Gérin^{1,3}, and Pierre Lesaffre^{1,3}

¹ Laboratoire de radioastronomie, LERMA, Observatoire de Paris, École Normale Supérieure, PSL Research University, CNRS, UMR 8112, 75005 Paris, France

e-mail: valeska.valdivia@lra.ens.fr

² Laboratoire AIM, Paris-Saclay, CEA/IRFU/Sap - CNRS - Université Paris Diderot, 91191 Gif-sur-Yvette Cedex, France

e-mail: patrick.hennebelle@lra.ens.fr

³ Sorbonne Universités, UPMC Univ. Paris 06, UMR 8112, LERMA, Paris, France, F-75005

Received Month dd, yyyy; accepted December 16, 2015

ABSTRACT

Context. H₂ is the simplest and the most abundant molecule in the interstellar medium (ISM), and its formation precedes the formation of other molecules.

Aims. Understanding the dynamical influence of the environment and the interplay between the thermal processes related to the formation and destruction of H₂ and the structure of the cloud is mandatory to understand correctly the observations of H₂.

Methods. We perform high resolution magnetohydrodynamical colliding flow simulations with the adaptive mesh refinement code RAMSES in which the physics of H₂ has been included. We compare the simulation results with various observations of the H₂ molecule, including the column densities of excited rotational levels.

Results. Due to a combination of thermal pressure, ram pressure and gravity, the clouds produced at the converging point of HI streams are highly inhomogeneous. H₂ molecules quickly form in relatively dense clumps and spread into the diffuse interclump gas. This in particular leads to the existence of significant abundances of H₂ in the diffuse and warm gas that lies in between clumps. Simulations and observations show similar trends, specially for the HI-to-H₂ transition (H₂ fraction vs total hydrogen column density). Moreover the abundances of excited rotational levels, calculated at equilibrium in the simulations turn out to be very similar to the observed abundances inferred from *FUSE* results. This is a direct consequence of the presence of the H₂ enriched diffuse and warm gas.

Conclusions. Our simulations, which self-consistently form molecular clouds out of the diffuse atomic gas, show that H₂ rapidly forms in the dense clumps and, due to the complex structure of molecular clouds, quickly spreads at lower densities. Consequently a significant fraction of warm H₂ exists in the low density gas. This warm H₂ leads to column densities of excited rotational levels close to the observed ones likely revealing the complex intermix between the warm and the cold gas in molecular clouds. This suggests that the 2-phase structure of molecular clouds is an essential ingredient to fully understand molecular hydrogen in these objects.

Key words. H₂- molecular clouds – ISM – column density – star formation

1. Introduction

It is well known that stars form in dense and self-gravitating molecular clouds and that the star formation rate per unit area (Σ_{SFR}) is on average relatively well correlated with the H₂ surface density (Σ_{H_2}) (Leroy et al. 2013; Lada et al. 2012; Wong & Blitz 2002; Bigiel et al. 2008).

Although H₂ is the simplest and the most abundant molecule in the interstellar medium (ISM), it is very hard to observe directly. Due to its homonuclear nature, H₂ lacks of permanent dipole and only weak quadrupolar transitions are allowed, moreover excitation energies are very high and require very high temperatures or strong ultraviolet (UV) fields to excite its rotational levels (Kennicutt & Evans 2012). H₂ can be observed in emission by infrared (IR) rovibrational transitions (Burton et al. 1992; Santangelo et al. 2014; Habart et al. 2011), or in absorption at far ultraviolet (UV) wavelengths from the Lyman and Werner bands. These bands were first observed by Spitzer & Jenkins (1975) using the *Copernicus* satellite. The *Far Ultraviolet Spectroscopic Explorer* (FUSE) (Moos et al. 2000) offered new perspectives on the study of H₂ in the ISM due to its sensitivity 10⁵ times higher than *Copernicus* in the far-UV part of the spectrum, providing measurements of H₂ column densities (total

column density of H₂ and for several rotational levels J) along translucent lines of sight (Wakker 2006; Sheffer et al. 2008).

While it seems to be clear that molecular gas is well correlated with star formation at different scales, how the gas becomes molecular is still an open issue. Since understanding the atomic-to-molecular hydrogen (HI-to-H₂) transition is of the highest importance for understanding the star forming process, numerous models have been developed (e.g. Krumholz et al. 2008; Sternberg et al. 2014) and seem able to reproduce many of the observed constraints. While extremely useful, these models leave aside the dynamical aspects of H₂ formation. In particular, the question of the relatively long time scale that is needed to form the H₂ molecules has been for many years difficult to reconcile with short-living and quickly forming molecular clouds. Indeed the typical time scale for H₂ formation is on the order of 10⁹yr/ n (Hollenbach et al. 1971), which would lead for molecular clouds of mean densities of the order of 10-100 cm⁻³ (Blitz & Shu 1980) to ages larger than 10 Myr. However, Glover & Mac Low (2007a) and Glover & Mac Low (2007b), who have been simulating the formation of molecular hydrogen in supersonic clouds, show that H₂ can form relatively quickly in the dense clumps induced by the shocks, leading to a time scale

significantly shorter (typically of about 3 Myr). Recently, Micic et al. (2012) explored the influence of the turbulent forcing and show that it has a significant influence on the timescale of H₂ formation. This is because compressible forcing leads to denser clumps than solenoidal forcing for which the motions are less compressible. This clearly shows that dynamics is playing an important role in the process of HI-to-H₂ transition, at least at the scale of a molecular cloud.

In the Milky-Way most of the molecular hydrogen is in the form of low temperature gas, nevertheless different observations have brought to light the existence of large amounts of fairly warm H₂ in the ISM (Valentijn & van der Werf 1999; Verstraete et al. 1999). Gry et al. (2002) and Lacour et al. (2005) have shown that the H₂ excitation resulting from UV pumping and from H₂ formation cannot account for the observed population of H₂ excited levels ($J > 2$). Excited H₂ is likely explained by the presence of a warm and turbulent layer associated to the molecular cloud. But in such warm gas, characterized by very low densities ($n_{\text{H}} \approx 1 - 10 \text{ cm}^{-3}$) and very high temperatures ($T \approx 10^{3-4} \text{ K}$), H₂ formation on grain surfaces becomes negligible therefore leading to an apparent contradiction. Recently, Godard et al. (2009) have been investigating the possibility that warm H₂ could form during intermittent high energy dissipation events such as vortices and shocks. They show in particular that under plausible assumptions regarding the distributions of these events, the observed abundance of excited H₂ molecules could be reproduced. Another possibility to explain the abundance of these excited H₂ molecules is that they could be formed in dense gas and then transported in more diffuse and warmer medium. This possibility has been investigated by Lesaffre et al. (2007) using a 1D model and a prescription to take into account the turbulent diffusion between the phases. In particular, they find that the abundance of H₂ molecules at low density and high temperature increases with the turbulent diffusion efficiency.

Therefore while different in nature, previous works (Glover & Mac Low 2007a,b; Lesaffre et al. 2007; Godard et al. 2009) consistently found that the formation of H₂ is significantly influenced by the dynamics of the flow in which it forms. Although the exact mechanism that leads to the formation of molecular clouds is still under investigation, it seems unavoidable to consider converging streams of diffuse gas (e.g. Hennebelle & Falgarone 2012; Dobbs et al. 2014). What exactly triggers these flows is not fully elucidated yet but is likely due a combination of gravity, large scale turbulence and large scale shell expansion. Another important issue is the thermodynamical state of the gas. The diffuse gas out of which molecular clouds form, is most likely a mixture of phases made of warm and cold atomic hydrogen (HI) and even possibly somewhat diffuse molecular gas. Such multiphase medium presents large temperature variations (typically from 8000 K to less than 50 K). This makes the dynamics of the flow significantly different from isothermal or nearly isothermal flow (see Audit & Hennebelle 2010, for a comparison between barotropic and 2-phase flows). Moreover the 2-phase nature of the diffuse atomic medium has been found to persist in molecular clouds (Hennebelle et al. 2008; Heitsch et al. 2008a; Banerjee et al. 2009; Vázquez-Semadeni et al. 2010; Inoue & Inutsuka 2012). This in particular produces a medium in which supersonic clumps of cold gas, are embedded into a diffuse phase of subsonic warm gas. Consequently, the question arises: what are the consequences of the multiphase nature of a molecular cloud onto the formation of H₂? Clearly, various processes may happen. First of all, the dense clumps are continuously forming and accreting out of the diffuse gas because molecular clouds keep accreting. Secondly, some of the

H₂ formed at high density is likely to be spread in low density, high temperature gas because of the phase exchanges.

In this work, we present numerical simulations using a simple model for H₂ formation within a dynamically evolving turbulent molecular cloud formed through colliding streams of atomic gas. Such flows, sometimes called colliding flows, have been widely used to study the formation of molecular clouds because they represent a good compromise between the need to assemble the diffuse material from the large scales and the need to describe accurately the small scales within the molecular clouds (Hennebelle & Pérault 1999; Ballesteros-Paredes et al. 1999; Heitsch et al. 2006; Vázquez-Semadeni et al. 2006; Clark et al. 2012). The content of this paper is as follows: in section 2 we present the governing equations and the physical processes such as H₂ formation. In section 3 we describe the numerical setup that we use to perform the simulations. In section 4 we present the results of our simulations, first describing the general structure of the cloud and then focussing on the H₂ distribution. We perform a few complementary calculations which aim at understanding better the physical mechanisms at play in the simulations. Then in section 5 we compare our results with various observations which have quantified the abundance of H₂ and find very reasonable agreements. Finally in section 6 we summarize and discuss the implications of our work.

2. Physical processes

2.1. Governing fluid equations

We consider the usual compressive magnetohydrodynamical equations that govern the behavior of the gas. These equations written in their conservative form are:

$$\frac{\partial \rho}{\partial t} + \nabla \cdot (\rho \mathbf{v}) = 0, \quad (1)$$

$$\frac{\partial \rho \mathbf{v}}{\partial t} + \nabla \cdot (\rho \mathbf{v} \mathbf{v} - \mathbf{B} \mathbf{B}) + \nabla P = -\rho \nabla \phi, \quad (2)$$

$$\frac{\partial E}{\partial t} + \nabla \cdot [(E + P) \mathbf{v} - \mathbf{B}(\mathbf{B} \mathbf{v})] = -\rho \mathcal{L}, \quad (3)$$

$$\frac{\partial \mathbf{B}}{\partial t} + \nabla \cdot (\mathbf{v} \mathbf{B} - \mathbf{B} \mathbf{v}) = 0, \quad (4)$$

$$\nabla^2 \phi = 4\pi G \rho \quad (5)$$

where ρ , \mathbf{v} , \mathbf{B} , P , E , ϕ are, respectively, the mass density, the velocity field, the magnetic field, the total energy and the gravitational potential of the gas, \mathcal{L} is the net loss function which describes gas cooling and heating.

2.2. Chemistry of H₂

The fluid equations (1-5) are complemented by an equation to describe the formation of the H₂ molecules

$$\frac{\partial n_{\text{H}_2}}{\partial t} + \nabla \cdot (n_{\text{H}_2} \mathbf{v}) = k_{\text{form}} n(n - 2n_{\text{H}_2}) - k_{\text{ph}} n_{\text{H}_2}, \quad (6)$$

where n is the total hydrogen density, n_{H_2} represents the density of H₂, k_{form} and k_{ph} represent respectively the formation and the destruction rates of H₂.

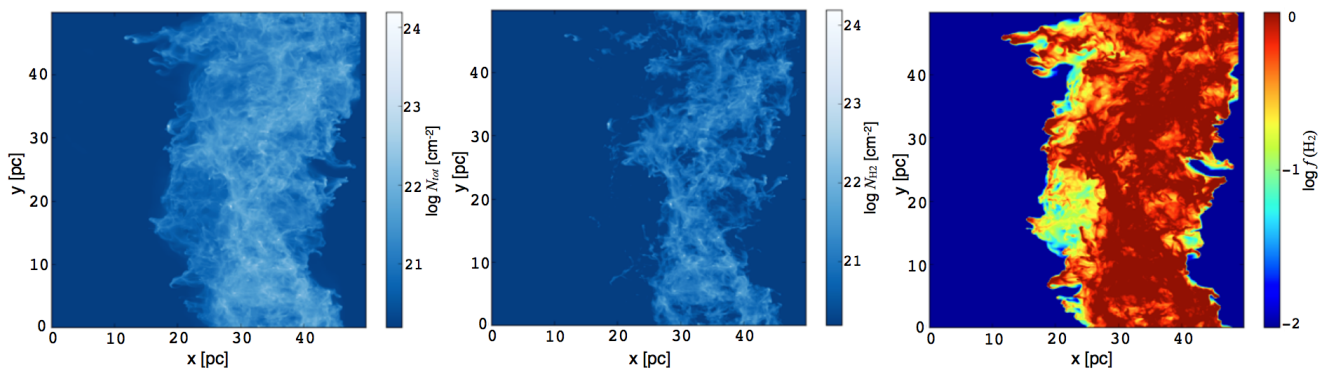


Fig. 1. Column density maps. Total hydrogen column density map (left), H₂ column density map (center), and molecular fraction (right). The gas enters the box from the left and right sides (x -axis), and the conditions for the other faces are periodic. The gas is compressed along the x -direction and the cloud forms toward the middle of the box.

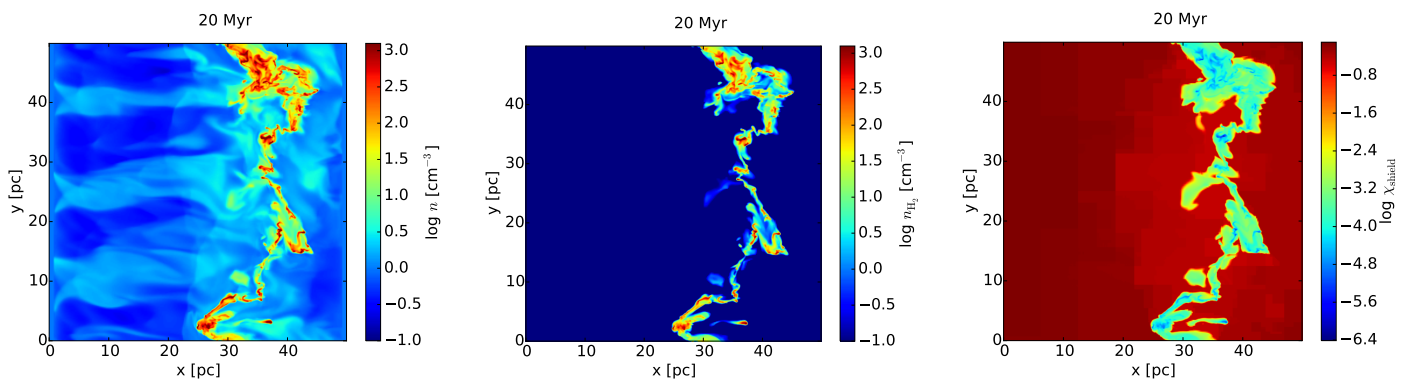


Fig. 2. Slices cut through the mid-plane. The panel on the left shows the total number density of hydrogen nucleons, the panel on the center shows the number density of molecular hydrogen (on the same scale), and the panel on the right shows the mean shielding factor for the H₂ photodissociation rate coefficient, calculated as $\langle \exp(-\tau_{d,1000}) f_{\text{shield}} \rangle$.

2.2.1. H₂ formation

When two hydrogen atoms encounter each other in gas phase, they cannot radiate the excess of energy due to the lack of electric dipole moment, and so forth H₂ formation in gas phase is negligible. Nowadays it is widely accepted that H₂ is formed through grain catalysis (Hollenbach & Salpeter 1971; Gould & Salpeter 1963). Hydrogen atoms can adsorb on the grain surfaces and encounter another hydrogen atom to form a H₂ molecule through two mechanisms: Langmuir-Hinshelwood, where atoms are physisorbed (efficient in the shielded gas), and Eley-Rideal, or chemisorption (efficient on warm grains) (Le Bourlot et al. 2012; Bron et al. 2014). The detailed physical description of these two mechanisms is complex and the numerical treatment is computationally expensive. For this reason we adopted a simpler description for H₂ formation on grain surfaces, given by the following mean formation rate:

$$k_{\text{form},0} = 3 \times 10^{-17} \text{ cm}^3 \text{ s}^{-1} \quad (7)$$

this rate was first derived by Jura (1974), using *Copernicus* observations and confirmed by Gry et al. (2002) using *FUSE* observations. The formation rate depends on the local gas temperature and on the adsorption properties of the grain, so this value is corrected by the dependence on temperature and by a sticking coefficient:

$$k_{\text{form}} = k_{\text{form},0} \sqrt{\frac{T}{100 \text{ K}}} \times S(T), \quad (8)$$

$S(T)$ is the empirical expression for the sticking coefficient of hydrogen atoms on the grain surface as described in Le Bourlot

et al. (2012):

$$S(T) = \frac{1}{1 + \left(\frac{T}{T_2}\right)^\beta}, \quad (9)$$

where we use the same fitting values as Bron et al. (2014), namely $T_2 = 464 \text{ K}$, and $\beta = 1.5$.

2.2.2. H₂ destruction

The main mechanism that destroys the H₂ molecule is the photodissociation by absorption of UV photons in the 912 - 1100 Å range (Lyman and Werner transitions). In optically thin gas, in presence of a UV field of strength G_0 , H₂ is photodissociated at a rate (Draine & Bertoldi 1996):

$$k_{\text{ph},0} = 3.3 \times 10^{-11} G_0 \text{ s}^{-1}, \quad (10)$$

but the H₂ gas can protect itself against photodissociation by two shielding effects. The first shielding effect is the *continuous dust absorption*, while the second effect is the line absorption due to other H₂ molecules, called *self-shielding*. Draine & Bertoldi (1996) show that the photodissociation rate can be written:

$$k_{\text{ph}} = e^{-\tau_{d,1000}} f_{\text{shield}}(\mathcal{N}_{\text{H}_2}) k_{\text{ph},0}. \quad (11)$$

The first term is the effect of the dust. Here $\tau_{d,1000} = \sigma_{d,1000} \mathcal{N}_{\text{tot}}$ is the optical depth along a line of sight ($\sigma_{d,1000} = 2 \times 10^{-21} \text{ cm}^2$ is the effective attenuation cross section for dust grains at $\lambda = 1000 \text{ Å}$ and \mathcal{N}_{tot} is the total column density of hydrogen). The

second term is the self-shielding factor and we use the same approximation:

$$f_{\text{shield}} = \frac{0.965}{(1+x/b_5)^2} + \frac{0.035}{(1+x)^{1/2}} \exp(-8.5 \times 10^{-4} (1+x)^{1/2}), \quad (12)$$

where $x = N_{\text{H}_2}/5 \times 10^{14} \text{ cm}^{-2}$, $b_5 = b/10^5 \text{ cm s}^{-1}$, where b is the Doppler broadening parameter, which is typically 2 km s^{-1} , but it can reach values as large as 10 km s^{-1} (Shull et al. 2000). We assume that the turbulent contribution dominates, then we use $b = 2 \text{ km s}^{-1}$ (see Appendix B for the influence of this choice on the shielding coefficient).

2.3. Thermal Processes

For the heating and cooling of the gas, we perform the same treatment as our previous work (Valdivia & Hennebelle 2014) (see also Audit & Hennebelle 2005), described in this section and that we called the standard heating and cooling, to which we have added the thermal feedback from H_2 , described in Sect. 2.3.1.

The dominant heating process in the gas is the due to the ultraviolet flux from the interstellar radiation field (ISRF) through the photoelectric effect on grains (Bakes & Tielens 1994; Wolfire et al. 1995), where we use the effective UV field strength, calculated using our attenuation factor χ for the UV field. We also include the heating by cosmic rays (Goldsmith 2001), which is important in well shielded regions.

The primary coolant at low temperature is the $^2P_{3/2} \rightarrow ^2P_{1/2}$ [CII] fine-structure transition at $158 \mu\text{m}$ (Launay & Roueff 1977; Hayes & Nussbaumer 1984; Wolfire et al. 1995). At higher temperature, fine-structure levels of OI can be excited and thus contribute to the cooling of the gas. We include the [OI] $63 \mu\text{m}$ and $146 \mu\text{m}$ line emission (Flower et al. 1986; Tielens 2005; Wolfire et al. 2003). For the Lyman α emission, that becomes dominant at high temperatures, we use the classical expression of Spitzer (1978). We also include the cooling by electron recombination onto dust grains using the prescription of Wolfire et al. (1995, 2003), and Bakes & Tielens (1994). Note that strictly speaking the present cooling function does not include molecular cooling in spite of the large densities reached in the simulation. It should however be noted that it leads to temperature which are entirely reasonable even at high densities and therefore appears to be sufficiently accurate in particular given that we are not explicitly solving for the formation of molecules apart from H_2 (see Levrier et al. 2012, for a quantitative estimate).

2.3.1. Thermal feedback from H_2

To the atomic cooling, described before, we added the molecular cooling by H_2 lines and the heating by H_2 formation and destruction.

During the H_2 formation process, about 4.5 eV are released. The distribution of this energy into translational energy, H_2 internal energy (rotational and vibrational excitation) and into the grain heating is not well known, and the fraction of this energy that actually heats the gas varies from one author to another (Le Bourlot et al. 2012; Glover & Mac Low 2007a). We consider an equipartition of the energy, so $1/3$ of the energy released goes into heating the gas:

$$\Gamma_{\text{form}} = 2.4 \times 10^{-12} k_{\text{form}} n_{\text{H}} n_{\text{H}} \text{ erg s}^{-1} \text{ cm}^{-3} \quad (13)$$

H_2 photodissociation provides an additional heating source. Following Black & Dalgarno (1977) and Glover & Mac Low

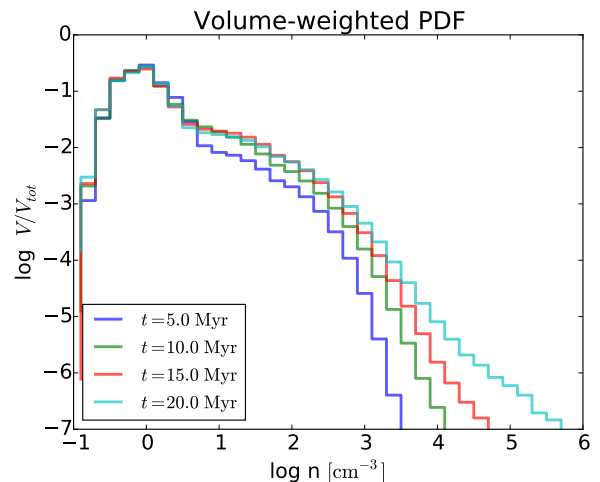


Fig. 3. Density PDF evolution. Color lines show the density PDF at $t = 5$ (blue), 10 (green), 15 (red), and 20 Myr (light blue).

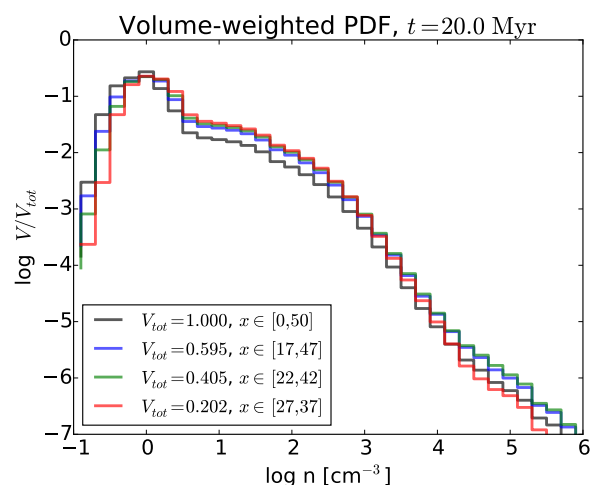


Fig. 4. Volume filling factor as a function of density in different regions. V_{tot} is the volume fraction of each region.

(2007a), we assume 0.4 eV released into the gas per photodissociation:

$$\Gamma_{\text{ph}} = 6.4 \times 10^{-13} k_{\text{ph}} n_{\text{H}_2} \text{ erg s}^{-1} \text{ cm}^{-3} \quad (14)$$

H_2 contributes to the cooling of the gas through line emission and it can become important for the diffuse medium under certain conditions (Glover & Clark 2014; Gnedin & Kravtsov 2011). As H_2 is a homonuclear molecule, only quadrupolar transitions are allowed and thus, the ortho and para states can be treated independently. In our simulations we adopt the cooling function from Le Bourlot et al. (1999). This is a function of temperature, total density, $n(\text{HI})/n(\text{H}_2)$ relative abundance, and of the ortho-to-para- H_2 ratio (OPR), and it considers transitions between the first 51 rovibrational energy levels. As the cooling function is quite insensitive to the OPR, we fixed it to 3 for simplicity.

3. Numerical setup and initial conditions

As already discussed, colliding flows are a practical ansatz to gather matter to form a molecular cloud (Inoue & Inutsuka 2012; Audit & Hennebelle 2005; Vázquez-Semadeni et al. 2007;

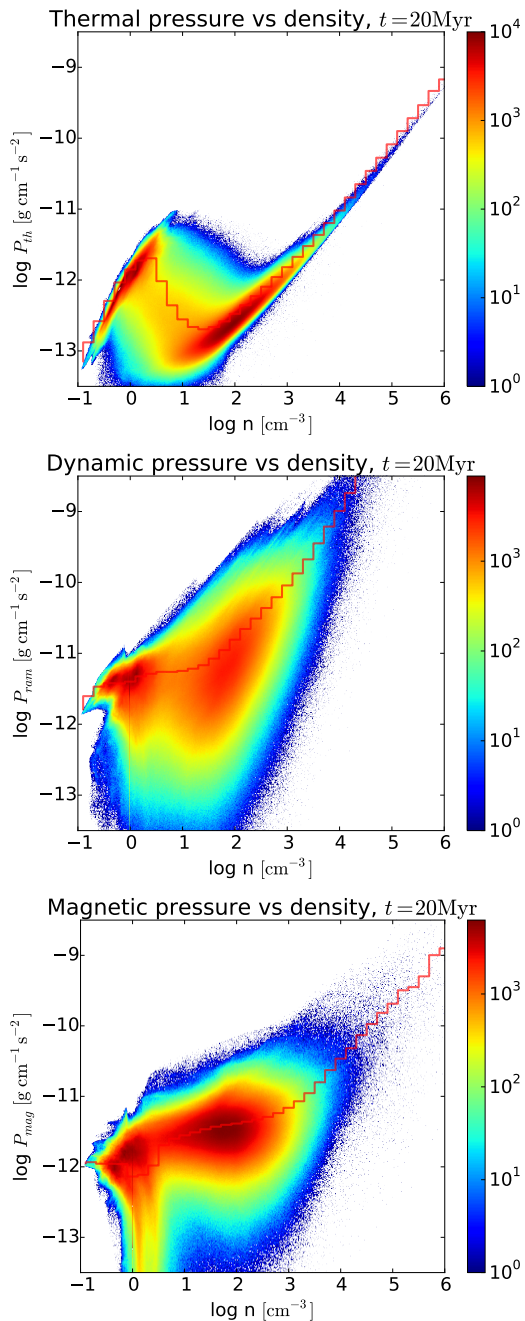


Fig. 5. The top panel shows the thermal pressure, $P_{th} = nkT$, the middle panel shows the ram pressure, $P_{ram} = \rho V^2$, while the bottom panel shows the magnetic pressure, $P_{mag} = B^2/8\pi$ in the simulation box. The red line shows the mean value per density bin. The color scale indicates the number of points.

Heitsch et al. 2005, 2006, 2008b; Micic et al. 2013) in order to mimic large scale converging flows, as in Galactic spiral arms or in super-bubble collisions.

3.1. General setup

The setup is very similar to Valdivia & Hennebelle (2014). The size of the simulation box is $L = 50$ pc and it is initially uniformly filled with atomic gas, with initial number density $n_{tot} = 1$ cm⁻³ and initial temperature $T = 8000$ K. Atomic gas, with the same number density and temperature, is injected

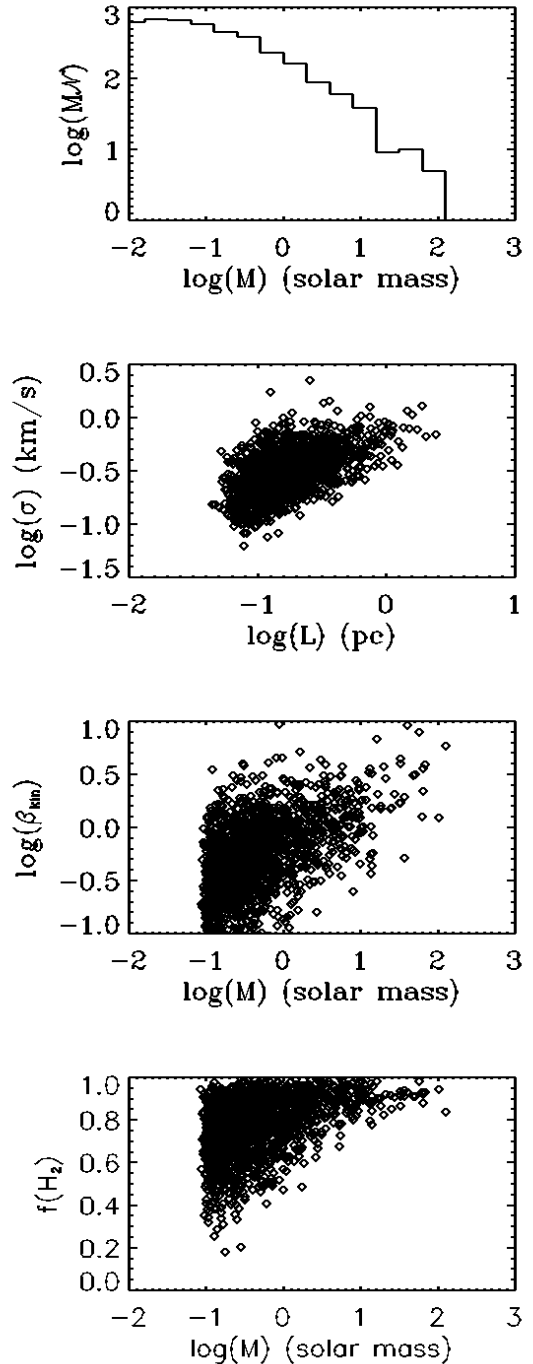


Fig. 6. Statistics of clumps. The top panel shows the mass spectrum, the second panel their internal velocity dispersion as a function of size, the third panel the kinetic $\beta = P_{ram}/P_{mag}$ and the bottom panel displays the H₂ fraction as a function of mass.

from the left and right faces of the box with an average velocity $V_0 = 15$ km s⁻¹, aligned with the x -axis, that is modulated by a function of amplitude $\epsilon = 0.5$, producing a slightly turbulent profile, as in Audit & Hennebelle (2005). We use periodic boundary conditions for the remaining faces. The gas is initially uniformly magnetized, with a moderate magnetic field (~ 2.5 μ G) aligned with the inflowing gas. This configuration avoids boundary issues and facilitates the building of the cloud. Introducing an angle between the magnetic and the velocity fields would be more

realistic, but in this very simplified framework requires relatively small angles (Hennebelle & Pérault 2000; Körtgen & Banerjee 2015; Inoue & Inutsuka 2012).

3.2. Radiative transfer and dust shielding

Molecular clouds are embedded in the interstellar radiation field (ISRF), which is supposed to be isotropic and constant throughout the space (Habing 1968). The whole simulation is embedded in an external and isotropic UV field, supposed to be monochromatic, of strength $G_0 = 1.7$ in Habing units, that heats the gas. UV photons are assumed to enter the computational box from all directions and undergo interactions with dust grains in their pathways before reaching any cell. The intensity of the UV field varies from one point to another according to the dust shielding factor χ , which is calculated at each point of the simulation box for each timestep using our *tree-based method*, fully described in Valdivia & Hennebelle (2014). Hence, the strength of the local UV field, after dust shielding, can be written $\bar{G}_0 = \chi G_0$, where $\chi = \langle e^{-2.5A_V} \rangle = \langle e^{-1.3 \times 10^{-21} N_{\text{tot}}} \rangle$, is the mean shielding factor due to dust. This mean value is calculated using a fixed number of directions. In our previous work (Valdivia & Hennebelle 2014) we have shown that the number of directions is not crucial for the dynamical evolution of the cloud, thus, for a matter of simplicity and numerical efficiency, we used 12 directions ($M = 3$ intervals for the polar angle and $N = 4$ for the azimuthal angle) which has turned out to be an excellent compromise between accuracy and efficiency.

We have adapted the code to also compute the self-shielding (stated by Eq. 12). More precisely, along each direction we compute not only the total gas density but also the H_2 column density from which we compute the shielding coefficient, f_{shield} , and the extinction due to dust, $\tau_{d,1000}$. Since the UV flux is assumed to be isotropic, the final photodissociation rate is obtained by taking the mean value over all directions. We define χ_{shield} as

$$\chi_{\text{shield}} = \frac{k_{\text{ph}}}{k_{\text{ph},0}} = \langle e^{-\tau_{d,1000}} f_{\text{shield}}(N_{\text{H}_2}) \rangle. \quad (15)$$

3.3. Numerical resolution and runs performed

To perform our simulations we employ the adaptive mesh refinement code RAMSES (Teyssier 2002; Fromang et al. 2006). RAMSES solves the MHD equations using the HLLD Riemann solvers. It preserves the nullity of the divergence of the magnetic field thanks to the use of a staggered mesh. To solve Eq. (6), we use operator splitting, solving first for the advection (which is identical to the conservation equation) and then subcycling to solve for the right-hand side. In AMR codes the refinement is done on a cell-by-cell basis. In our simulations, the refinement criterion is the density. When a cell reaches a given density threshold, it is split into eight smaller cells, each one having the same mass and volume. The process is repeated recursively until the maximum resolution is reached. In our fiducial run, we allow two AMR levels $\ell_{\text{min}} = 8$ and $\ell_{\text{max}} = 10$, leading to an equivalent numerical resolution of 1024^3 cells, and an effective spatial resolution of about 0.05 pc. For the first refinement level (from level $\ell = 8$ to $\ell = 9$) the density threshold is $n_{\text{thresh}} = 50 \text{ cm}^{-3}$ and for the next refinement, the density threshold is $n_{\text{thresh}} = 100 \text{ cm}^{-3}$. To investigate numerical convergence, a particularly crucial issue when chemistry is considered, we also perform a high resolution run for which the resolution is doubled (that is to say, using levels from 9 to 11 with the same refinement criterion).

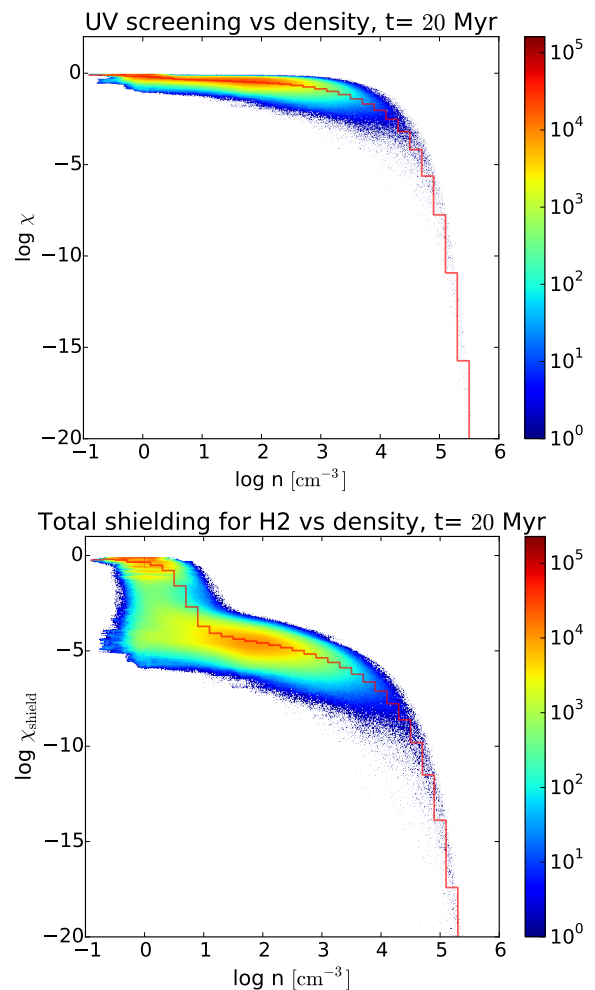


Fig. 7. UV screening factor vs density (top panel) and total shielding coefficient for H_2 vs density (bottom panel) at $t = 20$ Myr. The red line shows the mean value per density bin, and the color scale indicates the number of points.

We run our simulations for about 20 Myr. Note that these calculations are a little demanding because of the short timesteps induced by high temperatures, therefore it was not possible to run the high resolution simulations up to this point and this run goes up to 15 Myr. To check further for convergence, we have also performed low resolution runs (128^3 and 256^3 see Appendix) that we compare with our highest resolution simulations. We also perform complementary runs in which we modify the physics of H_2 formation in order to understand better how H_2 is formed. More precisely, in these runs we suppress H_2 formation above a certain density threshold.

4. Results

We now present the results of our calculations. We start first by discussing the general properties of the clouds as it is essential to understand in which context the hydrogen molecules form. Then we discuss the abundance and distribution of H_2 itself. Finally, we perform various complementary calculations aiming at better understanding in which conditions H_2 forms.

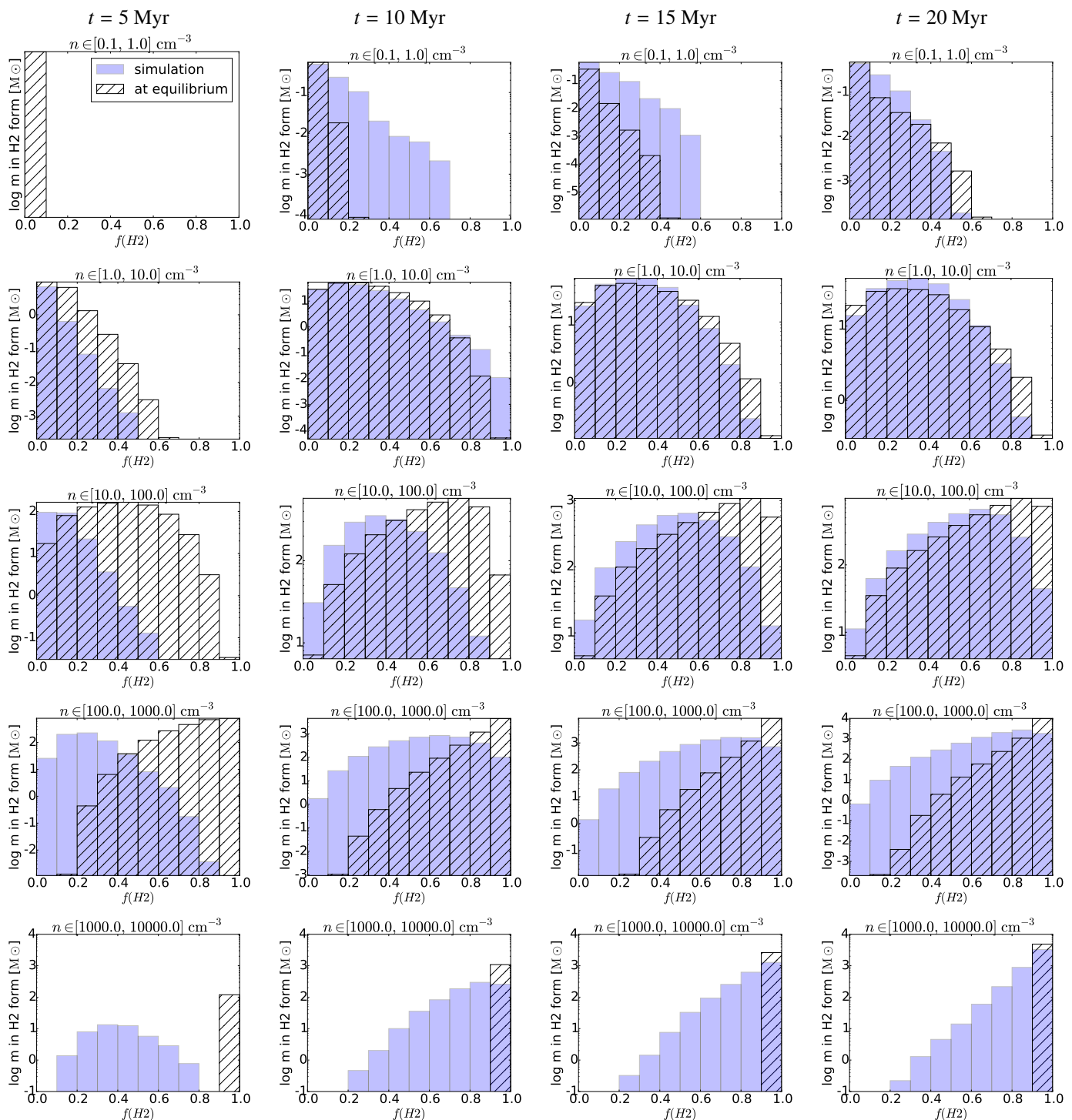


Fig. 10. Mass in H₂ form per density bin. Comparison between the simulation (blue) and the calculation at equilibrium (dashed) for different timesteps. From left to right: $t = 5, 10, 15,$ and 20 Myr. From top to bottom: density bins $n \in (0.1, 1), (1, 10), (10, 100), (100, 1000), (1000, 10000)$ [cm⁻³]. Note the change of vertical scale.

4.1. Qualitative description of the cloud

As many colliding flow calculations have been performed during the last decade, we do not attempt here to display all the steps that the flow is experiencing (see references above for accurate descriptions), so we quickly summarize the main steps. First, the WNM flows collide and this triggers the transition for a fraction

of the gas into moderately dense gas¹, that is to say densities on the order of 100-1000 cm⁻³ as a consequence of the thermal instability and ram pressure. Second, as enough gas has been accumulated, gravity becomes important and triggers infall, first at small scale and then at larger ones. This leads to a continuous increase of the dense gas fraction.

¹ if the incoming flow is fast enough a collision is not even necessary as it is the case for example in the study presented by Koyama & Inutsuka (2002)

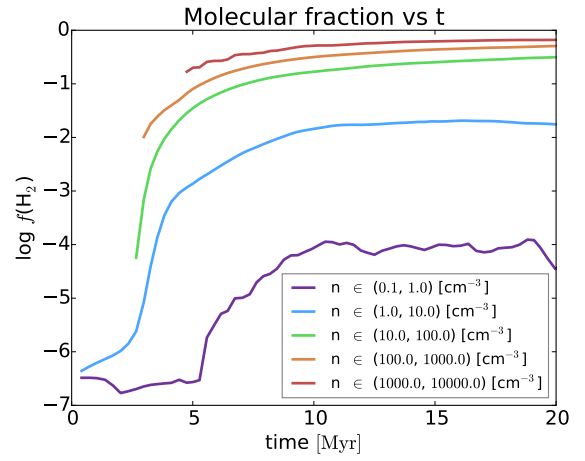
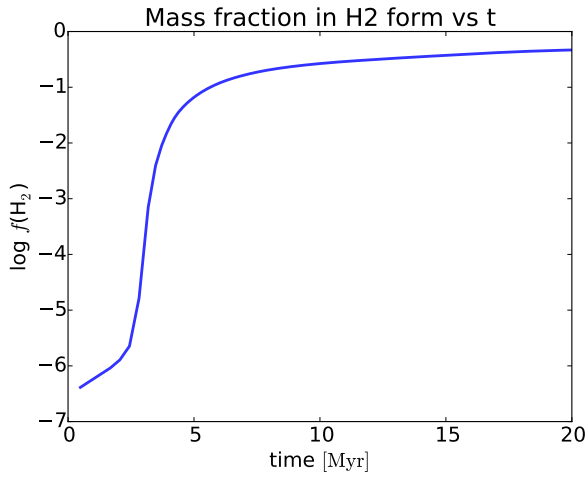


Fig. 8. Evolution of the molecular fraction in the simulation box as a function of time .

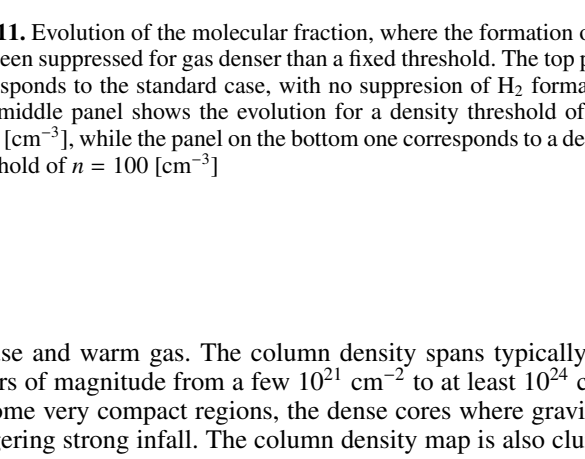
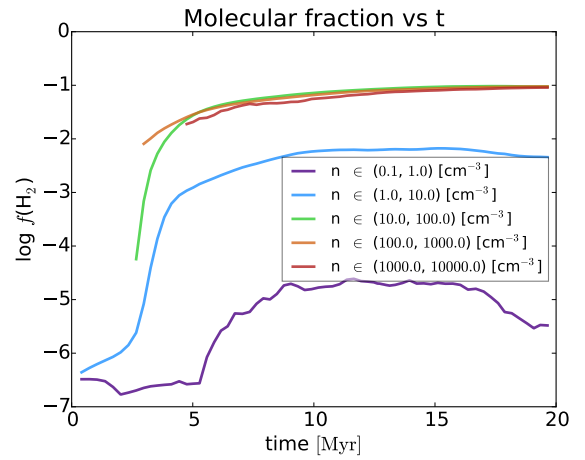
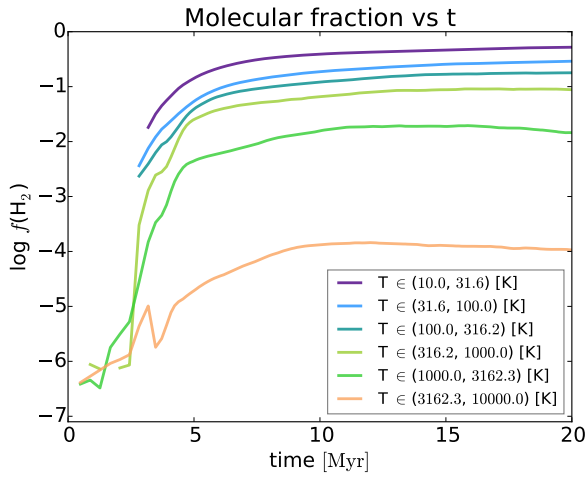
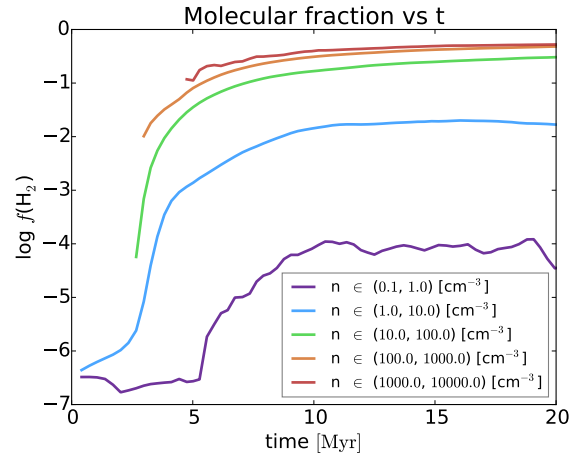
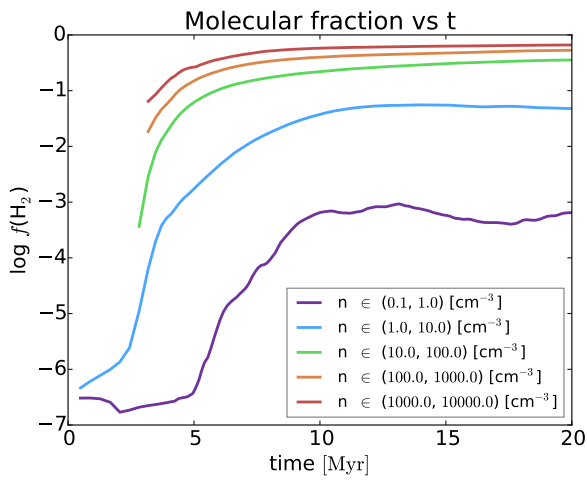


Fig. 9. Molecular fraction evolution. On the top: per density bin (from purple to red the density increases), on the bottom: per temperature bin (the temperature increases from purple to salmon).

Left panels of Figs. 1 and 2 show respectively the column density along the z -direction and a density cut in the xy plane at time 20 Myr. As will be seen below, this corresponds to a phase where gravity is already playing a significant role. As can be seen from the density cut, the flow is very fragmented. The dense gas is organized in dense clumps which are embedded in

diffuse and warm gas. The column density spans typically 2-3 orders of magnitude from a few 10^{21} cm^{-2} to at least 10^{24} cm^{-2} in some very compact regions, the dense cores where gravity is triggering strong infall. The column density map is also clumpy although less obviously structured than the density cut.

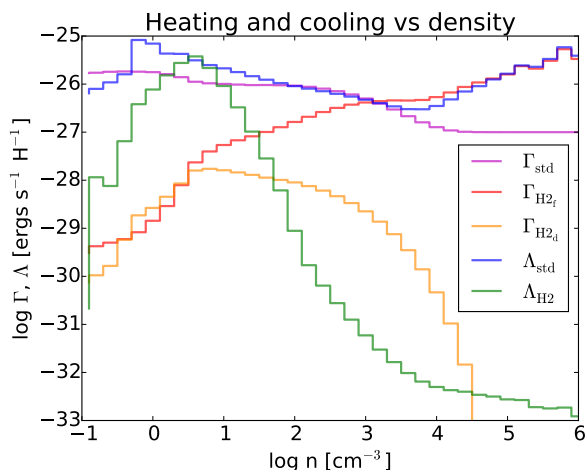


Fig. 12. Various cooling and heating contributions as a function of density. As can be seen H₂ does not have a dominant influence except at densities of about 4 cm⁻³ where H₂ cooling (green line) becomes comparable to the standard ISM cooling (blue line) and at high densities where the heating by H₂ formation (red line) is significant (but without modifying substantially the temperature).

4.1.1. Density PDF and volume filling factor

In many respects the density distribution is an essential cloud property which reveals the dynamical state of the cloud and strongly influences the formation of H₂.

Figure 3 shows the density probability distribution function (PDF) at time 5, 10, 15 and 20 Myr. The peak at low density ($n \simeq 1 \text{ cm}^{-3}$) is simply a consequence of the initial, and boundary conditions (which inject WNM from the boundaries), the rest, at higher densities, represents the cold phase, whose formation has been triggered by the thermal instability. Because of the supersonic turbulence that develops in the cold gas, the density PDF is broad and presents a lognormal shape (Kritsuk et al. 2007; Federrath et al. 2008). At later times, more cold gas accumulates and the PDF broadens. It is seen that the high density tail tends to become less steep. At intermediate densities ($\rho \sim 10^3\text{-}10^4 \text{ cm}^{-3}$) the shape is compatible with a power-law with an exponent between -1 and -2. This is typical of what has been found in super-sonic turbulent simulations which include gravity (Kritsuk et al. 2011). At very high densities ($> 10^4 - 10^5 \text{ cm}^{-3}$), the density field flattens. This is because, as we are not using sink particles, the very dense gas piles up and accumulate within few grid cells. This feature is thus a numerical artefact and represents a limit of the simulations.

Figure 4 shows the density PDF for different computational box regions at time 20 Myr. The four lines shows the results for four different box regions (as shown in the label). The black line shows the whole box while the red line is limited to the densest regions of the computational box. The volume filling factor is clearly dominated by the warm and diffuse gas. Selecting gas of densities $n < 3 \text{ cm}^{-3}$, we find that it typically occupies 70% for the region located between $x = 27$ and $x = 37$ (85% for the whole computational box). The dense gas, even in the densest region, occupies only a tiny fraction, for example we find that the gas denser than 100 cm^{-3} has a filling factor of about 3% (respectively 1.5% for the whole box). The remaining 26% (13%) are filled with gas of densities between 3 and 100 cm^{-3} . Thus we conclude that the interclump medium which occupies most of the volume, is itself made with two components, a warm gas that is similar to the standard WNM but can be a bit denser and a

cold gas that is similar to the CNM but contains, as will be seen later, a significant fraction of H₂. They typically occupy about 70% and 25% percent of the volume respectively.

4.1.2. Pressure of various phases

Another important diagnostic to characterize the dynamics of a medium are the different pressures. Figure 5 shows the thermal, P_{th} , dynamical, P_{ram} , and magnetic, P_{mag} , pressures equal to respectively $P_{th} = nkT$, $P_{ram} = \rho V^2$ and $P_{mag} = B^2/8\pi$.

As can be seen the dynamical pressure dominates the thermal one by typically one to two orders of magnitude in the dense gas ($n > 10 \text{ cm}^{-3}$) while they are more comparable in the diffuse gas. The magnetic pressure lies inbetween the two, with values a few times larger than the thermal one. P_{ram} and P_{mag} increase with density and at densities on the order of $n \simeq 10^3 \text{ cm}^{-3}$, they are about one order of magnitude larger than their mean values at $n \simeq 10 \text{ cm}^{-3}$. Therefore while the low density gas which fills the volume provides some confining pressure, it has a limited influence on the clumps.

Altogether these results indicate that the molecular cloud produced in this calculation can be described by density fluctuations or clumps, induced by both ram pressure and gravity. The clumps occupy a tiny fraction of the volume which is filled by a mixture of warm diffuse and dense HI gas (occupying respectively a fraction $>70\%$ and $>20\%$ of the volume). This low density material is feeding the clumps, which grow in mass. This picture is in good agreement with the measurement performed by Williams et al. (1995), who found that the interclump medium has typically a density of a few particles per cm⁻³ and a large velocity dispersion of several km s⁻¹.

4.1.3. Statistics of clumps

As the cloud is organized in clumps, we further quantify the simulations by providing some statistics. To identify the clumps, we use a density threshold of 1000 cm^{-3} and a friends-of-friends algorithm. This structure is important for the chemistry evolution since, at the edge of clumps very significant density and temperature gradients arise. Fig. 6 shows the mass spectrum, the velocity dispersion and the kinetic β parameter (that is to say P_{ram}/P_{mag}) of the clumps. As can be seen the mass spectrum for masses above a few $0.1 M_{\odot}$ presents a powerlaw with an index of about -1.7, which is very similar to what has been shown in related works (e.g. Audit & Hennebelle 2010; Heitsch et al. 2008b). The velocity dispersion within clumps as a function of their size is about $\sigma \simeq 1 \text{ km s}^{-1}(L/1\text{pc})$, which is close to the Larson relation (Larson 1981; Hennebelle & Falgarone 2012). From third panel, it is seen that the kinetic β parameter is typically of the order of, or slightly below 1, showing that the magnetic field plays an important role within the clumps.

4.2. Molecular hydrogen

We now turn to the H₂ abundance discussion. Middle and right panels of Fig. 1 show the H₂ column density and molecular abundance, $f(\text{H}_2) = 2n(\text{H}_2)/n$. As expected the high column density regions are dominated by the H₂ molecules and values of $f(\text{H}_2)$ close to 1 are obtained there. Obviously in the outer parts of the cloud, the values of $f(\text{H}_2)$ are significantly lower.

4.2.1. The UV screening factor

Middle and right panels of Fig. 2 respectively shows a cut of $n(\text{H}_2)$ and the value of the shielding parameter, $\chi_{\text{shield}} = k_{\text{ph}}/k_{\text{ph},0}$. This latter steeply decreases when entering inside the cloud where it takes values on the order of 10^{-3} . A comparison between the density cut with $k_{\text{ph}}/k_{\text{ph},0}$ reveals that there are regions of diffuse material in which the shielding parameter is low. This is because these regions are surrounded by dense gas in which H_2 is abundant therefore providing an efficient self-shielding. As a consequence, there are low density regions which contain a relatively high abundance of H_2 (see left and middle panels of Fig. 2).

A more quantitative statement can be drawn from Fig. 7 that displays the distribution of the dust shielding, χ (top panel) and of the total shielding χ_{shield} as a function of density (bottom panel). As expected most low density cells, are associated to χ values that are close to 1, that is to say are weakly shielded. There is however a fraction of them which present values of χ_{shield} as small as 10^{-5} . At higher densities, the mean value of χ decreases with a steep drop between $n \approx 10^3$ and 10^4 cm^{-3} which correspond to the point where the dust significantly absorbed the UV external field. For the total shielding, a steep drop is observed at about 10 cm^{-3} . There is however a broad scatter, which increases from $n = 1$ to $n = 10^4 \text{ cm}^{-3}$ for the dust shielding and tends to decrease for the total shielding χ_{shield} . This indicates that the mean value of χ_{shield} is not a sufficient information to quantify the abundance of H_2 expected at a given density. This is a clear consequence of the complex cloud structure. Since χ_{shield} plays a key role in the formation of H_2 , this complex distribution certainly makes molecular hydrogen formation in a multiphase turbulent cloud, a complicated issue.

4.2.2. Global evolution of molecular hydrogen

Figure 8 shows $f(\text{H}_2)$, the mean molecular fraction within the whole cloud, as a function of time. During the first 5 Myr, $f(\text{H}_2)$ exponentially increases from nearly 0 to about ≈ 0.1 . After this phase, $f(\text{H}_2)$ keeps increasing in a more steady almost linear way. Near 15 Myr, about 40% of the gas is in H_2 molecules. Since, as discussed before, the cloud is rather inhomogeneous in density and temperature, we have also plotted the time evolution per bins of density and temperature. The corresponding curves are displayed in Fig. 9. As expected, the total distribution closely follows the values of the densest bins, that is to say corresponding to densities larger than $100\text{-}1000 \text{ cm}^{-3}$. For these densities, the timescale for H_2 formation is thus of a few ($\approx 6 - 8$) Myr. As recalled previously, this typical timescale is about $10^9/n \text{ yr}$. Therefore the timescale we observe in the simulation agrees well with this scaling. Altogether, this is in good agreement with the results of Glover & Mac Low (2007a,b) which found that H_2 could be formed quickly in molecular clouds because it preferentially forms into clumps that are significantly denser than the rest of the cloud. In the present case, the mean density of our cloud at time 5-10 Myr would be about $10\text{-}100 \text{ cm}^{-3}$ (depending exactly which area is selected) and this would lead to timescale for H_2 formation on the order of 10 to 100 Myr.

What is somewhat more surprising is the relatively short amount of time (≈ 10 Myrs) after which there is a significant amount of H_2 in low density gas ($n \approx 1 - 10 \text{ cm}^{-3}$). The expected timescale for H_2 formation in this density range would be about 10^8 Myr. As can be seen from Fig. 9, the behavior of $f(\text{H}_2)$ is similar, although not identical, to the behavior at higher densities. There is a fast increase followed by a slowly increasing

phase. There is however a change of slope at about 4 Myr that is different from the higher density evolution. The steady evolution starts at about 8 Myr instead of 5-6 Myr for the denser regions. This suggests that the presence of H_2 at low density is triggered by formation of H_2 in the dense gas. This can happen in various non-exclusive ways. First of all, some dense gas can expand back and mix with diffuse gas. This may happen either through a sonic expansion, through evaporation or through numerical diffusion. Second of all, some of the diffuse gas may be surrounded by dense gas in which $f(\text{H}_2)$ is large and therefore has a low χ_{shield} . Below we attempt to analyse further these mechanisms.

Finally, we note from the bottom panel of Fig. 9 that there is a small (1-10%) but nevertheless non negligible fraction of H_2 within relatively high temperature gas, i.e. $T > 300 \text{ K}$. Since H_2 is the first molecule involved to produce other molecules and since some of them, such as CH^+ , are formed through reactions with high activation barriers (on the order of 4300 K for CH^+ , see Agúndez et al. 2010), the presence of H_2 could have consequences for the production of these species as proposed in Lesaffre et al. (2007). In the same way, as discussed below, this warm H_2 contains molecules in excited high J rotational levels, which can therefore contribute to the gas cooling.

4.2.3. Detailed distribution of molecular hydrogen

To further quantify the distribution of H_2 in the cloud, we display histograms of $f(\text{H}_2)$ per bin of density (Fig. 10). We also draw in the same panel the distribution $f(\text{H}_2)$ obtained at equilibrium. Knowing the density, n , the temperature, T and the shielding factor, χ_{shield} , we solve Eq. (6) at equilibrium. Note that this distribution is not fully self-consistent since the value of χ_{shield} should in principle be recalculated to be consistent with this equilibrium distribution (this would imply performing several iterations). In practice, the goal here is simply to compare with the time-dependent distribution to gain insight on the H_2 production mechanisms, and it is therefore easier to have exactly the same formation and destruction rates.

In particular the equilibrium distribution is expected to be different from the time-dependent one for at least two main reasons. First, since the H_2 formation time-scale is somewhat long, if the time-dependent $f(\text{H}_2)$ lies below the equilibrium one, it will indicate that what has limited the H_2 abundance is the time to form the molecule. Second, if the time-dependent $f(\text{H}_2)$ is above the equilibrium value, it will indicate that $f(\text{H}_2)$ has increased because of an enrichment coming from denser gas. As discussed above this could operate through the expansion or the evaporation of cold clumps, a process that we call turbulent diffusion, or through numerical diffusion. The latter is quantified in the appendix by performing convergence studies which suggest that it remains limited. Another possibility is that the H_2 excess has been produced during a phase where the fluid particle was more shielded by the surrounding material and therefore the UV field was lower. The two effects are probably acting simultaneously and are difficult to disentangle.

At time 5 Myr (left panels), all density bins show an excess of the equilibrium distribution with respect to the time-dependent one. This is clearly due to the long time-scale needed to form H_2 . As time goes on, the differences between the equilibrium and time-dependent distributions become less important. For example the two distributions are obviously closer at time 20 Myr (right panels) than at time 5 Myr. However, they are not identical. Since all distributions at time 15 Myr and 20 Myr are similar, the persistence of the differences between the equilibrium and time-dependent distributions, indicates that this is likely the

result of a stationary situation. Most likely it reflects the accretion process, that is to say HI gas (possibly mixed with a fraction of H₂) is continuously being accreted within denser clumps and therefore the dense gas does not become fully molecular. This interpretation is also consistent with the fact that the effect is more pronounced for the fourth density bin (line 4) than for the fifth and highest one (line 5). Looking now at the lowest density bin (first line), one finds the reverse effect at time 10 and 15 Myr, the time-dependent distribution dominates the equilibrium one. This is most likely an effect of the turbulent diffusion. From the low mass contained in this low density bin, this however remains a limited effect.

The second density bin (line 2), which corresponds to n between 1 and 10 cm⁻³ is a little puzzling. No significant differences are seen between the two distributions, which is surprising. One possibility is that various effects compensate. That is to say the time delay to form H₂ (clearly visible for the 3 denser density bins) may be compensated by an enrichment from the denser gas. This is indeed possibly happening for the second density bin at time 20 Myr (fourth column, second line) where it is seen that there is overall a small excess of time-dependent H₂ but that for $f(\text{H}_2) > 0.7$ the equilibrium distribution dominates.

4.2.4. Spatial fluctuations

As a complement to the time evolution of $f(\text{H}_2)$, it is also worth to investigate the spatial fluctuations at a given time. In this respect, the clumps constitute natural entities to study the spatial variations. The bottom panel of Fig. 6 shows $f(\text{H}_2)$ within the clumps. For the most massive clumps, the value of $f(\text{H}_2)$ is close to 1 and the dispersion remains weak. On the contrary, for the less massive clumps, the dispersion becomes very significant and the value of $f(\text{H}_2)$ can be in some circumstances rather low. This shows that clump histories, that is to say their ages and the local UV flux in which they grow, have a major influence on $f(\text{H}_2)$.

4.2.5. Further analysis of H₂ formation

In order to better quantify the interdependence of the different density bins, we have conducted three complementary low resolution runs for which the formation of H₂ is suppressed (k_{form} is set to zero) above a given density threshold. Figure 11 displays the result. In the top panel, no threshold is applied. In the middle and bottom panels a threshold of 1000 cm⁻³ and 100 cm⁻³, respectively, is applied. As can be seen with the threshold 1000 cm⁻³, the values of $f(\text{H}_2)$ are not significantly changed except for the highest density range (for $n > 1000$ cm⁻³). On the other hand, with a threshold 100 cm⁻³, the values of $f(\text{H}_2)$ decrease by a factor of about 3 for all density bins. This clearly shows that most of the H₂ molecules in the low density gas form at a density of a few 100 cm⁻³. While the shielding provided by molecules in gas denser than this value could contribute to enhance the more diffuse gas, the filling factor of the dense gas is too small to affect significantly the diffuse gas that has a much larger filling factor (see Fig. 4). Therefore we conclude that the H₂ abundance within the low density gas (<100 cm⁻³), is likely a consequence of turbulent mixing and gas exchange between diffuse and dense gas.

4.3. Thermal balance

To quantify the influence of the H₂ molecule on thermodynamics, we present the contributions of the various heating and cool-

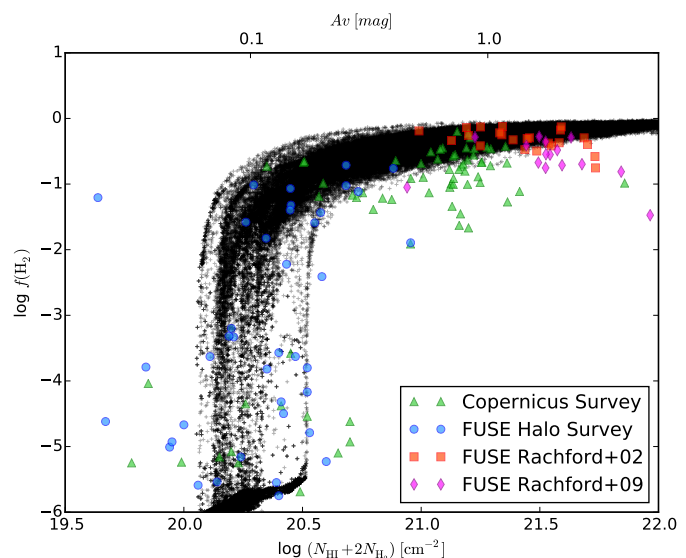


Fig. 13. Molecular fraction as a function of total hydrogen column density. Comparison with *Copernicus* survey (Savage et al. 1977), and *FUSE* (Gillmon et al. 2006; Rachford et al. 2002, 2009).

ing terms to the thermal balance as a function of density. Figure 12 shows the standard ISM cooling (blue curve) as well as the cooling by H₂ (green curve). As can be seen, the latter remains overall below the former except at density of about 3-5 cm⁻³ where they become comparable. At densities above 3×10^4 cm⁻³ the "standard" heating curve (magenta) is dominated by the heating caused by cosmic rays, reaching the intermediate value for shielded gas proposed by Goldsmith (2001). While the heating due to H₂ destruction remains negligible at any density (orange curve), the heating due to its formation (red curve) turns out to be the dominant heating mechanism at high densities. This however does not affect very significantly the temperature which stays equal to about 10 K. It is also worth to note that at higher densities (above $\sim 10^5$ cm⁻³) other processes not included in our simulations can take over, as the collisions with dust grains and the cooling by other molecular lines, such as CO.

Finally, as can be seen for densities between 1 to ~ 50 cm⁻³, the cooling dominates the heating by a factor of a few. This indicates that there is another source of heating equal to the difference, which turns out to be due to the mechanical energy dissipation. This latter therefore appears to have a contribution comparable to the UV heating. This explains why warm gas is actually able to survive within molecular clouds. In the same way that density is much larger than in the rest of the ISM, kinetic energy is also larger and provides a significant heating (e.g. Hennebelle & Inutsuka 2006).

5. Confrontation to observations

We now compare our results with various observations which fall in two categories. The first ones have attempted to measure the molecular fraction, i.e. the total column density of H₂ with respect to the total column density. The second ones have been measuring the excited levels of H₂, therefore presumably tracing high temperature gas. These two sets of observations are therefore complementary and very informative.

5.1. Molecular fraction vs column density

The H_2 column density has been estimated along several lines of sight mainly (though not exclusively) with the *Copernicus* satellite (Savage et al. 1977) and *FUSE* observatory (Gillmon et al. 2006; Rachford et al. 2002, 2009). These observations probe lines of sight spanning a wide range of column densities and therefore constitute a good test for our simulations although a difference to keep in mind is that the lines of sight extracted from our simulations are all taken from a 50 pc region and therefore are more homogeneous than the observed lines of sight.

Figure 13 shows the molecular fraction $f(H_2)$ as a function of total column density for all lines of sight of the simulations (taken along the z -direction) and the available lines of sight reported in Gillmon et al. (2006), and Rachford et al. (2002, 2009). As can be seen, the simulation results and the observations agree rather well, many observational data directly fall into the same regions than simulated data. In particular, the two regimes, i.e. the vertical transition branch at column densities between 10^{20} and $3 \times 10^{20} \text{ cm}^{-2}$ as well as the higher column density region, are clearly seen both in observations and in the simulation.

This said, there are also data points which are not reproduced by any of the lines of sight from the simulations. This is particularly the case for column densities larger than $3 \times 10^{21} \text{ cm}^{-2}$ and for the *Copernicus* survey at column densities around $\approx 10^{21} \text{ cm}^{-2}$. The most likely explanation is that the UV flux is different from the standard value we assume in our study. Let us stress in particular that the measurements are done in absorption toward massive stars. As they are strong emitters of UV radiation, it may not be too surprising that our measurements lead to larger values of $f(H_2)$. A more quantitative estimate should entail a detailed modelling of every lines of sight including the UV flux in the regions of interest as well as specific cloud parameters, such as column densities. This is beyond the scope of the present paper.

5.2. Excited levels of H_2

We now turn to the comparison with the observations of rotational levels of the H_2 molecule, which require high temperatures to be excited.

As investigated by previous authors (Lacour et al. 2005; Godard et al. 2009), these data cannot be explained by pure UV excitation. While Lacour et al. (2005) concluded that to explain the observations, a warm layer associated to the cold gas should be present, Godard et al. (2009) performed detailed models entailing shocks or vortices. The general idea is that in such dissipative small scale structures, the temperature reaches high values because of the intense mechanical heating. Interestingly, Godard et al. (2009) obtained a nice agreement between their model and the data. Let us stress that the small dissipative scales which are determinant in these models, cannot be described in our simulations which have a limited resolution on the order of ≈ 0.1 pc. On the other hand, as our simulations contained large quantities of warm H_2 , it is worth investigating whether the inferred populations of excited H_2 can be quantitatively reproduced.

5.2.1. Calculation of population levels and column densities

We calculate the population of the first six rotational levels (J) of H_2 as in Flower et al. (1986), based on the Elitzur & Watson (1978) approach. This calculation is done in post-processing for all grid cells. It needs the total hydrogen number density, the H_2 number density, the He number density (we assume 10% of

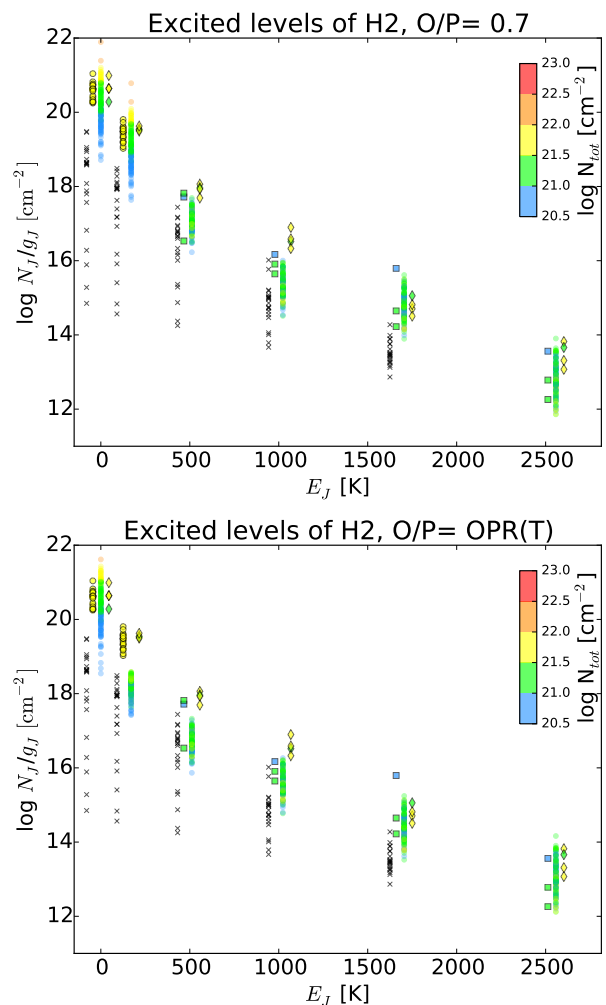


Fig. 14. H_2 population distribution along different lines of sight at time $t = 20$ Myr, using an ortho-to-para ratio of 0.7 (top), and at thermal equilibrium (bottom). The symbols correspond to the observational data of Wakker (2006) (cross), Rachford et al. (2002) (circle), Gry et al. (2002) (square) and Lacour et al. (2005) (diamond). Colors correspond to the total column density range.

total H), the temperature, and the ortho-to-para ratio (OPR). It supposes thermal equilibrium, and it includes spontaneous de-excitation, and collisional excitation by HI, by He, and by other H_2 molecules.

The OPR is not very well known in the ISM (e.g. Le Bourlot 2000) and may need a specific time-dependent treatment, which is beyond the scope of the paper. Even though the OPR of newly formed H_2 molecules is thought to take values close to 3 (Takahashi 2001), observations differ. In high density regions ($n(H_2) \sim 10^5 \text{ cm}^{-3}$) observations seem to favor values as low as 0.25 (Neufeld et al. 2006; Pagani et al. 2011; Dislaire et al. 2012), while in translucent clouds intermediate values close to 0.7 are preferred (Myers et al. 2015; Gry et al. 2002; Lacour et al. 2005; Nehmé et al. 2008; Ingalls et al. 2011; Rachford et al. 2009). As we investigate the role of low density gas regions in the distribution of excited rotational levels of H_2 , we assume an OPR= 0.7, suitable for translucent clouds as those produced in our simulations. We also consider, for comparison, an OPR given by thermal equilibrium, that reaches the statistical weight of 3 at high temperatures ($T \gtrsim 300$ K).

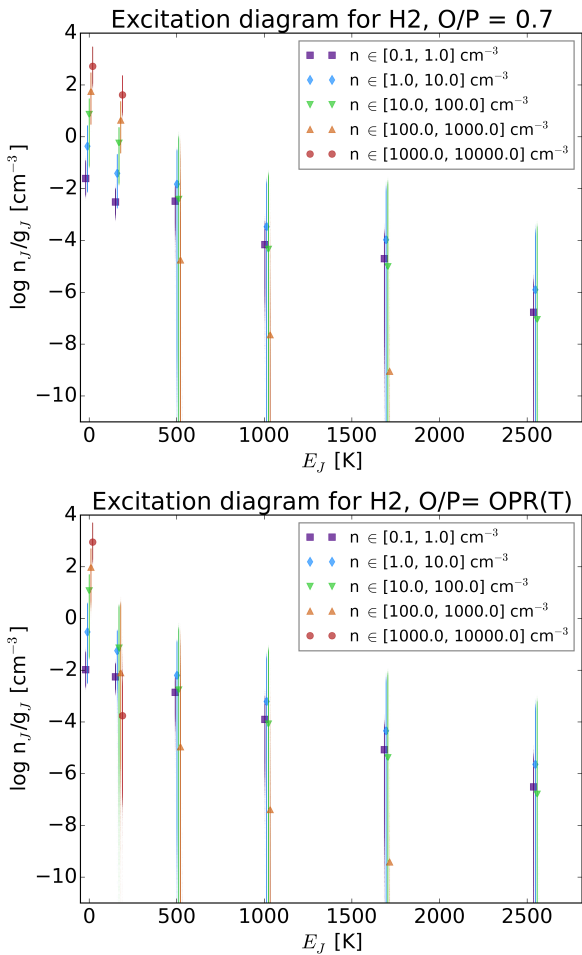


Fig. 15. H₂ level population distribution for individual cells in the simulation calculated at 20 Myr: using an ortho-to-para ratio OPR = 0.7 (top) and at thermal equilibrium (bottom).

Once we obtain the populations of the H₂ rotational levels, column density we integrate along several lines of sight in the z -direction.

5.2.2. Comparison with observed column densities

Figure 14 shows the distribution of the column densities corresponding to the various rotational levels in the simulation. The top panel shows results for OPR equal to 0.7 while the bottom one shows results for the thermal equilibrium assumption. The color coding shows the total column density of the corresponding line of sight. The symbols correspond to the observational data of Wakker (2006) (cross), Rachford et al. (2002) (circle), Gry et al. (2002) (square) and Lacour et al. (2005) (diamond).

The simulation results split into 2 groups of points, very low column densities coming from the WNM that is located outside the molecular cloud (blue points) and higher column densities (green and yellow points), which come from the gas belonging to the molecular cloud. For the $J = 0$ and 1 levels, the column densities are more or less proportional to the total column density. This is indeed expected since most of H₂ molecules are in one of these two levels. Their respective abundance significantly depends on the assumption used for the OPR. While there is about a factor 10 between the first two rotational levels for N_j/g_j when the OPR is equal to 0.7, it is almost a factor thousand when the OPR is assumed to be at thermal equilibrium.

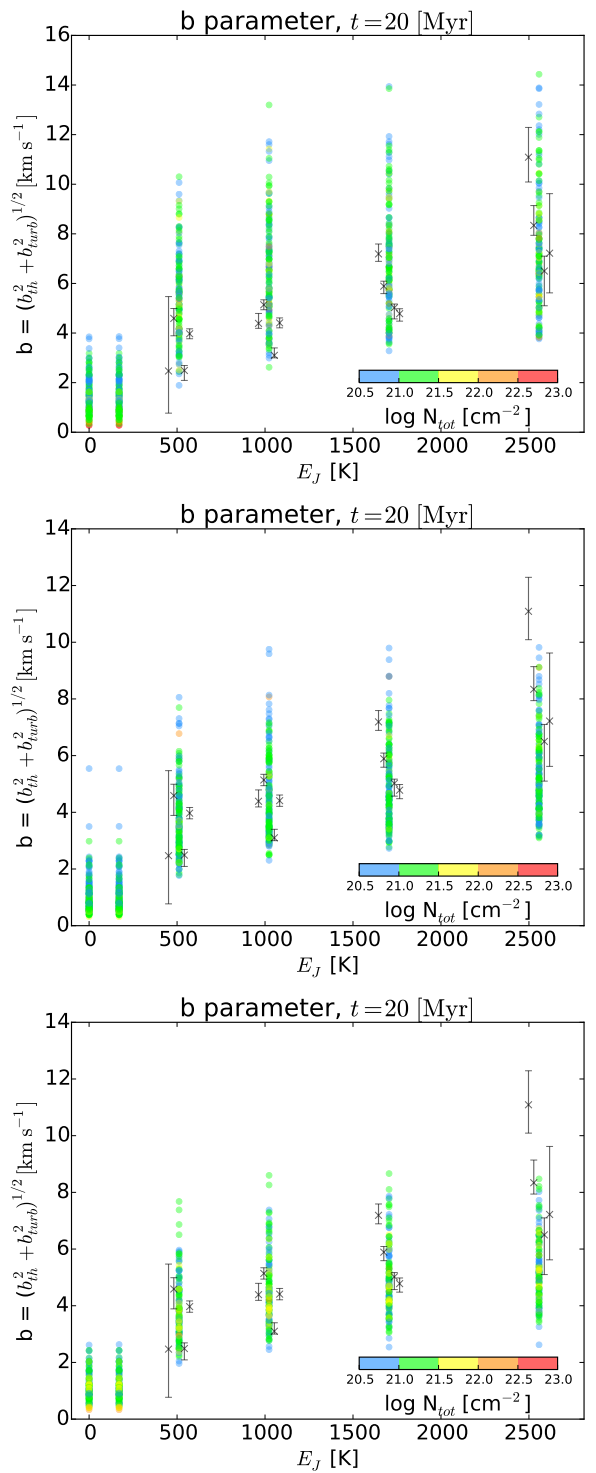


Fig. 16. b -parameter along several lines of sight for excited levels of H₂ and comparison with the data from Lacour et al. (2005). Top panel is for lines of sight along the x -axis, middle one is along y -axis and bottom panel along z -axis.

The situation is different for the higher levels. The largest column densities of the excited rotational levels do not correspond to the largest total hydrogen column densities and generally there is no obvious correlation between the two. This is due to the fact that the high J levels are coming from the warm gas (with temperatures between few hundreds and few thousands

Kelvin), which itself has a low column density and is largely independent of the cold gas.

The comparison with the observational data is very enlightening. Overall the agreement with the simulation results is very good. The observational data points have column densities which are very similar to the simulation data. The best agreement is found for the OPR= 0.7 case, for which simulation data points are slightly above the observational ones, while for an OPR at thermal equilibrium simulation data points are below. This probably suggests that the actual OPR is lying inbetween, being close to 0.7. There is a possible tension with some of the data of Gry et al. (2002) and Lacour et al. (2005) for $J = 2$, by a factor on the order of 3-10. If confirmed this would indicate that another mechanism, such as the one proposed by Godard et al. (2009) could operate and contribute to excite H_2 .

In order to understand what is the origin of the excited rotational levels in the simulation, Fig. 15 displays the mean density of the H_2 excited levels for five density bins as well as the complete distribution for the two OPR used in this work. Figure 15 shows that the choice of the OPR affects mainly the dense, and thus colder gas, which is the main contributor to the populations of the two first levels ($J = 0$ and $J = 1$). The OPR at thermal equilibrium for very dense and cold gas is close to zero, affecting dramatically the ratio between the populations of these two levels. At lower densities, in warmer gas, the OPR gets closer to 3, but the populations do not differ much from those calculated using OPR= 0.7. For the excited level the highest contributions are found in gas of total density between 1 and 10 cm^{-3} . Then, in roughly equal proportions, very diffuse gas with $n < 1 \text{ cm}^{-3}$ and moderately dense one (with n between 10 and 100 cm^{-3}) contribute to excited levels. It is worth recalling that the peak of the cooling contribution of H_2 , precisely lies in this density domain (see Fig. 12).

5.2.3. Velocity dispersion of individual rotational levels

So far the conclusion we can draw is that the population of the excited levels of H_2 ($J \geq 2$) is dominated by the warm H_2 that is interspersed between the cold and dense molecular clumps. This "layer" of warm gas is directly associated with the molecular cloud and agrees well with the proposition made by Lacour et al. (2005). Interestingly these authors made another interesting observation. They found that the width of the lines associated to the excited levels increases with J . In order to investigate whether our simulation exhibits the same trends, we have calculated the mean velocity dispersion along several (125 along each axis) lines of sight for each excited level. Figure 16 shows the mean Doppler broadening parameter, b , linked to the velocity dispersion σ by $b^2 = 2^{1/2}\sigma^2$, and where

$$\sigma^2 = \frac{\int \rho \left((v_i - \langle v_i \rangle)^2 + C_s^2 \right) dx}{\int \rho dx}, \quad (16)$$

where C_s is the local sound speed, v_i is the i component of the local velocity, and $\langle v_i \rangle$ is the mean velocity along the i -direction. Figure 16 displays the results. Since the colliding flow configuration is highly non-isotropic, we have calculated these velocity dispersion along x -axis (top panel), y -axis (middle panel) and z -axis (bottom panel). While a more accurate treatment would consist in simulating the line profiles and then applying the same algorithm that the authors used, this simple estimate is already illustrative. From σ^2 , we can infer the width of the line and the b parameter.

As can be seen the trends in the simulation and in the observations are similar. Higher J levels tends to be associated with larger b . Quantitatively the agreement is satisfying for the y and z -directions. As the observations, the simulated lines of sight present slightly larger velocity dispersion for higher J . The agreement is poor for the lines of sight along the x -direction as they present a dispersion that is too high with respect to the observations. This is most likely an artifact of the colliding flow configuration.

The trend of larger b for higher J stems for the fact that higher levels need warmer gas to be excited. Therefore the fluid elements, which are enriched in high rotational levels have larger temperatures and therefore larger velocity dispersions (since both are usually correlated).

Altogether these results suggest that the excited rotational level abundances reveal the complex structure of molecular clouds that is 2-phase in nature and entails warm gas deeply interspersed with the cold gas due to the mixing induced by turbulence.

6. Conclusions

We have performed high resolution magneto-hydrodynamical simulations to describe the formation of molecular clouds out of diffuse atomic hydrogen streams. We particularly focus on the formation of the H_2 molecule itself using a tree-based approach to evaluate UV shielding (see Valdivia & Hennebelle 2014).

In accordance with previous works (Glover & Mac Low 2007a), we find that H_2 is able to form much faster than simple estimates, based on cloud mean density, would predict. This is because, since the clouds are supersonic and have a 2-phase structure, H_2 is produced in clumps which are much denser than the clouds on average.

Due to a combination of phase exchanges and high UV screening deep inside the multiphase molecular clouds (numerical convergence tests suggest that numerical diffusion is not responsible of this process), a significant fraction of H_2 develops even in the low density and warm interclump medium. This warm H_2 contributes to the thermal balance of the gas and in the range of density $3 - 10 \text{ cm}^{-3}$ its cooling rate is comparable to the standard cooling rate of the ISM.

Detailed comparisons with *Copernicus* and *FUSE* observations show good agreement overall. In particular the fraction of H_2 varies with the total gas column density in a very similar way showing a steep increase between column densities 10^{20} and $3 \times 10^{20} \text{ cm}^{-2}$ and a slow increase at larger column densities. There is however a trend for the high column densities regions to present H_2 fractions significantly below the values inferred from the simulations. This is a possible consequence of the constant UV flux assumed in this work. Interestingly, the column densities of the excited rotational levels obtained at thermal equilibrium reproduce fairly well the observations. This is a direct consequence of the presence of H_2 molecules in the warm interclump medium and suggests that the H_2 populations in excited levels reveal the 2-phase structure of molecular clouds.

Acknowledgements. We thank the anonymous referee for the critical reading and valuable comments. We thank J. Le Bourlot and B. Godard for the insightful discussions.

V.V. acknowledges support from a CNRS-CONICYT scholarship. This research has been partially funded by CONICYT and CNRS, according to the December 11, 2007 agreement.

P.H. acknowledges the financial support of the Agence National pour la Recherche through the COSMIS project. This research has received funding from the European Research Council under the European Community's Seventh Framework Program (FP7/2007-2013 Grant Agreement No. 306483).

M.G. and P.L. thank the French Program "Physique Chimie du Milieu Interstellaire" (PCMI)

This work was granted access to the HPC resources of MesoPSL financed by the Region Ile de France and the project Equip@Meso (reference ANR-10-EQPX-29-01) of the programme Investissements d'Avenir supervised by the Agence Nationale pour la Recherche

References

- Agúndez, M., Goicoechea, J. R., Cernicharo, J., Faure, A., & Roueff, E. 2010, *ApJ*, 713, 662
- Audit, E. & Hennebelle, P. 2005, *A&A*, 433, 1
- Audit, E. & Hennebelle, P. 2010, *A&A*, 511, A76
- Bakes, E. L. O. & Tielens, A. G. G. M. 1994, *ApJ*, 427, 822
- Ballesteros-Paredes, J., Vázquez-Semadeni, E., & Scalo, J. 1999, *ApJ*, 515, 286
- Banerjee, R., Vázquez-Semadeni, E., Hennebelle, P., & Klessen, R. S. 2009, *MNRAS*, 398, 1082
- Bigiel, F., Leroy, A., Walter, F., et al. 2008, *AJ*, 136, 2846
- Black, J. H. & Dalgarno, A. 1977, *ApJS*, 34, 405
- Blitz, L. & Shu, F. H. 1980, *ApJ*, 238, 148
- Bron, E., Le Bourlot, J., & Le Petit, F. 2014, *A&A*, 569, A100
- Burton, M. G., Hollenbach, D. J., & Tielens, A. G. G. 1992, *ApJ*, 399, 563
- Clark, P. C., Glover, S. C. O., Klessen, R. S., & Bonnell, I. A. 2012, *MNRAS*, 424, 2599
- Dislaire, V., Hily-Blant, P., Faure, A., et al. 2012, *A&A*, 537, A20
- Dobbs, C. L., Krumholz, M. R., Ballesteros-Paredes, J., et al. 2014, *Protostars and Planets VI*, 3
- Draine, B. T. & Bertoldi, F. 1996, *ApJ*, 468, 269
- Elitzur, M. & Watson, W. D. 1978, *A&A*, 70, 443
- Federrath, C. 2013, *MNRAS*, 436, 1245
- Federrath, C., Klessen, R. S., & Schmidt, W. 2008, *ApJ*, 688, L79
- Flower, D. R., Pineau-Des-Forets, G., & Hartquist, T. W. 1986, *MNRAS*, 218, 729
- Fromang, S., Hennebelle, P., & Teyssier, R. 2006, *A&A*, 457, 371
- Gillmon, K., Shull, J. M., Tumlinson, J., & Danforth, C. 2006, *ApJ*, 636, 891
- Glover, S. C. O. & Clark, P. C. 2014, *MNRAS*, 437, 9
- Glover, S. C. O. & Mac Low, M.-M. 2007a, *ApJS*, 169, 239
- Glover, S. C. O. & Mac Low, M.-M. 2007b, *ApJ*, 659, 1317
- Gnedin, N. Y. & Kravtsov, A. V. 2011, *ApJ*, 728, 88
- Godard, B., Falgarone, E., & Pineau Des Forêts, G. 2009, *A&A*, 495, 847
- Goldsmith, P. F. 2001, *ApJ*, 557, 736
- Gould, R. J. & Salpeter, E. E. 1963, *ApJ*, 138, 393
- Gry, C., Boulanger, F., Nehmé, C., et al. 2002, *A&A*, 391, 675
- Habart, E., Abergel, A., Boulanger, F., et al. 2011, *A&A*, 527, A122
- Habing, H. J. 1968, *Bull. Astron. Inst. Netherlands*, 19, 421
- Hayes, M. A. & Nussbaumer, H. 1984, *A&A*, 134, 193
- Heitsch, F., Burkert, A., Hartmann, L. W., Slyz, A. D., & Devriendt, J. E. G. 2005, *ApJ*, 633, L113
- Heitsch, F., Hartmann, L. W., & Burkert, A. 2008a, *ApJ*, 683, 786
- Heitsch, F., Hartmann, L. W., Slyz, A. D., Devriendt, J. E. G., & Burkert, A. 2008b, *ApJ*, 674, 316
- Heitsch, F., Slyz, A. D., Devriendt, J. E. G., Hartmann, L. W., & Burkert, A. 2006, *ApJ*, 648, 1052
- Hennebelle, P., Banerjee, R., Vázquez-Semadeni, E., Klessen, R. S., & Audit, E. 2008, *A&A*, 486, L43
- Hennebelle, P. & Falgarone, E. 2012, *A&A Rev.*, 20, 55
- Hennebelle, P. & Inutsuka, S.-i. 2006, *ApJ*, 647, 404
- Hennebelle, P. & Pérou, M. 1999, *A&A*, 351, 309
- Hennebelle, P. & Pérou, M. 2000, *A&A*, 359, 1124
- Hollenbach, D. & Salpeter, E. E. 1971, *ApJ*, 163, 155
- Hollenbach, D. J., Werner, M. W., & Salpeter, E. E. 1971, *ApJ*, 163, 165
- Ingalls, J. G., Bania, T. M., Boulanger, F., et al. 2011, *ApJ*, 743, 174
- Inoue, T. & Inutsuka, S.-i. 2012, *ApJ*, 759, 35
- Jura, M. 1974, *ApJ*, 191, 375
- Kennicutt, R. C. & Evans, N. J. 2012, *ARA&A*, 50, 531
- Körtgen, B. & Banerjee, R. 2015, *ArXiv e-prints*
- Koyama, H. & Inutsuka, S.-i. 2002, *ApJ*, 564, L97
- Kritsuk, A. G., Norman, M. L., Padoan, P., & Wagner, R. 2007, *ApJ*, 665, 416
- Kritsuk, A. G., Norman, M. L., & Wagner, R. 2011, *ApJ*, 727, L20
- Krumholz, M. R., McKee, C. F., & Tumlinson, J. 2008, *ApJ*, 689, 865
- Lacour, S., Ziskin, V., Hébrard, G., et al. 2005, *ApJ*, 627, 251
- Lada, C. J., Forbrich, J., Lombardi, M., & Alves, J. F. 2012, *ApJ*, 745, 190
- Larson, R. B. 1981, *MNRAS*, 194, 809
- Launay, J.-M. & Roueff, E. 1977, *Journal of Physics B Atomic Molecular Physics*, 10, 879
- Le Bourlot, J. 2000, *A&A*, 360, 656
- Le Bourlot, J., Le Petit, F., Pinto, C., Roueff, E., & Roy, F. 2012, *A&A*, 541, A76
- Le Bourlot, J., Pineau des Forêts, G., & Flower, D. R. 1999, *MNRAS*, 305, 802
- Leroy, A. K., Walter, F., Sandstrom, K., et al. 2013, *AJ*, 146, 19
- Lesaffre, P., Gerin, M., & Hennebelle, P. 2007, *A&A*, 469, 949
- Levrier, F., Le Petit, F., Hennebelle, P., et al. 2012, *A&A*, 544, A22
- Micic, M., Glover, S. C. O., Banerjee, R., & Klessen, R. S. 2013, *MNRAS*, 432, 626
- Micic, M., Glover, S. C. O., Federrath, C., & Klessen, R. S. 2012, *MNRAS*, 421, 2531
- Moos, H. W., Cash, W. C., Cowie, L. L., et al. 2000, *ApJ*, 538, L1
- Myers, A. T., McKee, C. F., & Li, P. S. 2015, *MNRAS*, 453, 2747
- Nehmé, C., Le Bourlot, J., Boulanger, F., Pineau Des Forêts, G., & Gry, C. 2008, *A&A*, 483, 485
- Neufeld, D. A., Melnick, G. J., Sonnentrucker, P., et al. 2006, *ApJ*, 649, 816
- Pagani, L., Roueff, E., & Lesaffre, P. 2011, *ApJ*, 739, L35
- Rachford, B. L., Snow, T. P., Destree, J. D., et al. 2009, *ApJS*, 180, 125
- Rachford, B. L., Snow, T. P., Tumlinson, J., et al. 2002, *ApJ*, 577, 221
- Santangelo, G., Antonucci, S., Nisini, B., et al. 2014, *A&A*, 569, L8
- Savage, B. D., Bohlin, R. C., Drake, J. F., & Budich, W. 1977, *ApJ*, 216, 291
- Sheffer, Y., Rogers, M., Federman, S. R., et al. 2008, *ApJ*, 687, 1075
- Shull, J. M., Tumlinson, J., Jenkins, E. B., et al. 2000, *ApJ*, 538, L73
- Spitzer, L. 1978, *Physical processes in the interstellar medium*
- Spitzer, Jr., L. & Jenkins, E. B. 1975, *ARA&A*, 13, 133
- Sternberg, A., Le Petit, F., Roueff, E., & Le Bourlot, J. 2014, *ApJ*, 790, 10
- Takahashi, J. 2001, *ApJ*, 561, 254
- Teyssier, R. 2002, *A&A*, 385, 337
- Tielens, A. G. G. M. 2005, *The Physics and Chemistry of the Interstellar Medium*
- Valdivia, V. & Hennebelle, P. 2014, *A&A*, 571, A46
- Valentijn, E. A. & van der Werf, P. P. 1999, *ApJ*, 522, L29
- Vázquez-Semadeni, E., Colín, P., Gómez, G. C., Ballesteros-Paredes, J., & Watson, A. W. 2010, *ApJ*, 715, 1302
- Vázquez-Semadeni, E., Gómez, G. C., Jappsen, A. K., et al. 2007, *ApJ*, 657, 870
- Vázquez-Semadeni, E., Ryu, D., Passot, T., González, R. F., & Gazol, A. 2006, *ApJ*, 643, 245
- Verstraete, L., Falgarone, E., Pineau des Forets, G., Flower, D., & Puget, J. L. 1999, in *ESA Special Publication, Vol. 427, The Universe as Seen by ISO*, ed. P. Cox & M. Kessler, 779
- Wakker, B. P. 2006, *ApJS*, 163, 282
- Williams, J. P., Blitz, L., & Stark, A. A. 1995, *ApJ*, 451, 252
- Wolfire, M. G., Hollenbach, D., McKee, C. F., Tielens, A. G. G. M., & Bakes, E. L. O. 1995, *ApJ*, 443, 152
- Wolfire, M. G., McKee, C. F., Hollenbach, D., & Tielens, A. G. G. M. 2003, *ApJ*, 587, 278
- Wong, T. & Blitz, L. 2002, *ApJ*, 569, 157

Appendix A: The issue of numerical convergence: resolution study

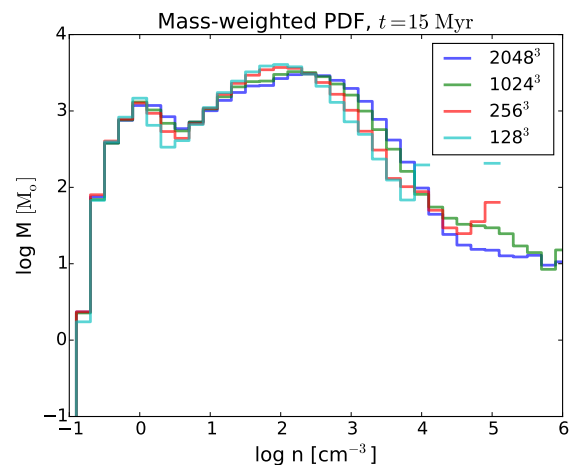


Fig. A.1. Mass-weighted density PDF for a series of numerical resolutions. While the discrepancy between low and high resolution runs is very significant. The difference between the resolution of the standard and high resolution runs is not very high except for the highest density bins, which contain little mass.

Numerical resolution is a crucial issue particularly in the context of chemistry. Here we present a comparison between runs of various resolutions.

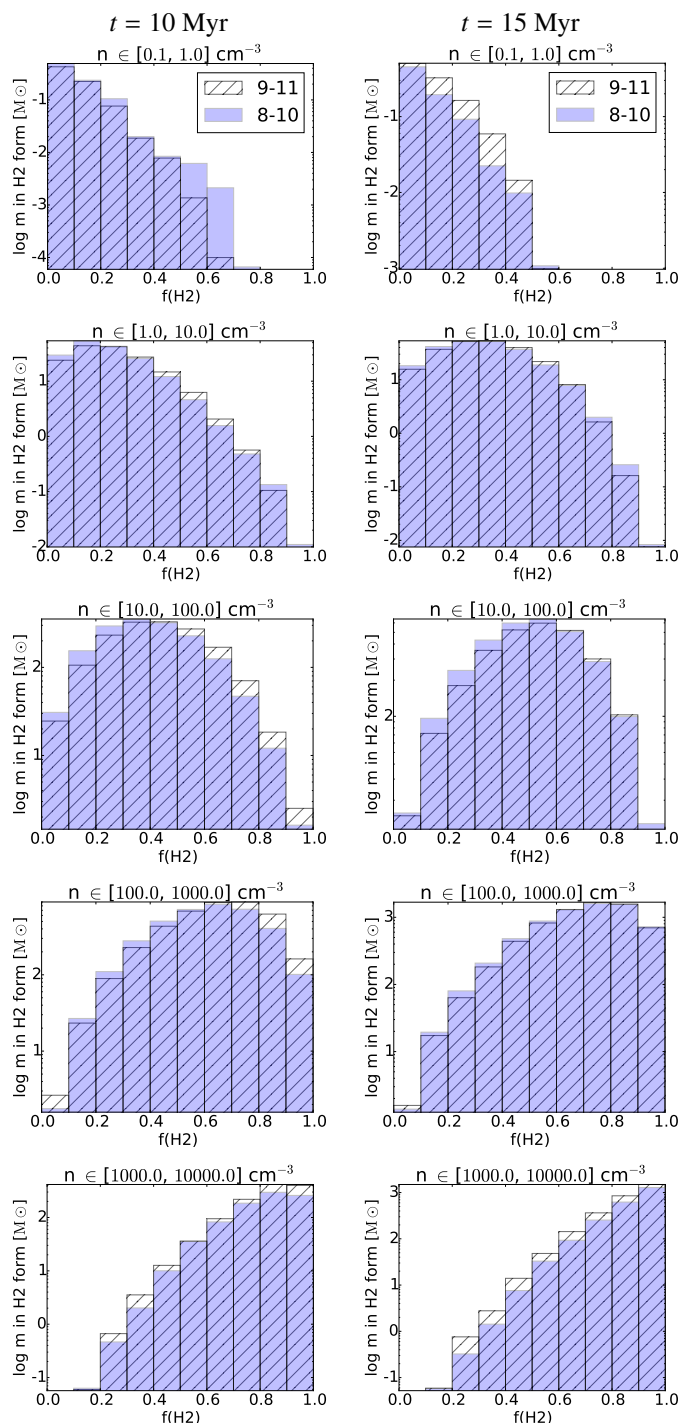


Fig. A.2. Mass in H_2 per density bin. Comparison between the standard resolution simulations (levels 8-10, in blue) and the high resolution one (levels 9-11, dashed) at time 10 and 15 Myr. From top to bottom: density bins $n \in (0.1, 1)$, $(1, 10)$, $(10, 100)$, $(100, 1000)$, $(1000, 10000)$ $[\text{cm}^{-3}]$. The differences between the two remain fairly limited showing that numerical convergence is not a too severe issue.

Figure A.1 shows the mass-weighted density PDF at time 15 Myr for 4 different resolutions, 128^3 , 256^3 , 1024^3 and 2048^3 (for the two last and higher resolutions this represents the highest effective resolution since AMR is used as described above). The density PDF of low resolution runs is quite different from the higher ones showing the importance of numerical resolu-

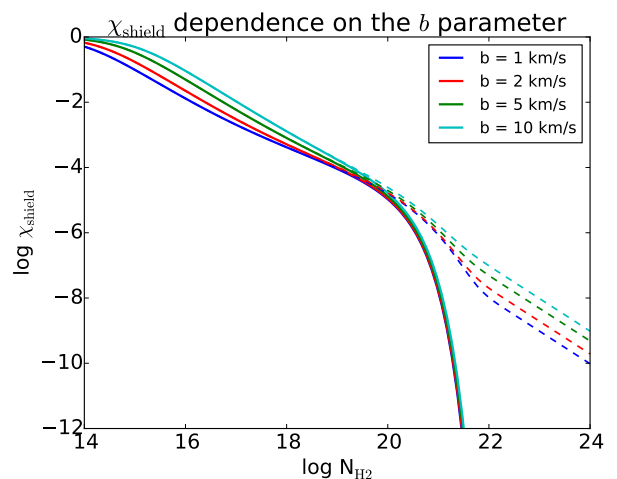


Fig. B.1. Total shielding coefficient for H_2 , χ_{shield} , as a function of total H_2 column density for several values of the b Doppler parameter. Dashed lines show the expected value in absence of shielding by dust.

tion. The two highest resolution runs present similar though not identical PDF. This suggests that for the highest resolution runs, numerical convergence for the density PDF is nearly reached although strictly speaking, it would be necessary to perform even higher resolution runs. This conclusion agrees well with the results of Federrath (2013) who find that for isothermal self-gravitating simulations, the density PDF converges for a resolution inbetween 1024^3 and 2048^3 .

Figure A.2 shows $f(\text{H}_2)$ distribution in 5 density bins at times 10 and 15 Myr for the standard and high resolution runs (effective 1024^3 and 2048^3 resolution). Overall the two simulations agree well. The differences are comparable to the differences found on the density PDF. In particular, this suggests that numerical diffusion is not primary responsible of the fraction of warm H_2 that we observe at low density (as discussed in Section 4.2).

Appendix B: Influence of the b Doppler parameter

Figure B.1 shows the dependence of the total shielding coefficient for H_2 (shielding by H_2 and by dust) on the b Doppler parameter as a function of total H_2 column density. The total column density has been approximated as $N_{\text{tot}} \approx 2 \times N_{\text{H}_2}$, which sets a lower limit to the influence of dust shielding. The χ_{shield} parameter varies within less than one order of magnitude for different b parameters ranging from 1 to 10 km s^{-1} . In the H_2 column density range of interest ($N_{\text{H}_2} \sim 10^{17} - 10^{22} \text{ cm}^{-2}$) all values are very similar. At higher column densities the shielding is dominated by dust.